Advanced Photonics Research

ADVANCED PHOTONICS RESEARCH Open Access

www.adpr-journal.com

RESEARCH ARTICLE OPEN ACCESS

Generation of Anisotropic Second-Harmonic Petal-Like Beams with $NbOBr_2$ Holograms

Jayanta Deka[1] | Jie Gao[2] | Xiaodong Yang[1]

[1]Department of Mechanical and Aerospace Engineering, Missouri University of Science and Technology, Rolla, MO, USA | [2]Department of Mechanical Engineering, Stony Brook University, Stony Brook, NY, USA

Correspondence: Jie Gao (jie.gao.5@stonybrook.edu) | Xiaodong Yang (yangxia@mst.edu)

Received: 16 November 2025 | **Revised:** 13 March 2026 | **Accepted:** 17 March 2026

Keywords: 2D materials | anisotropic response | petal-like beam | second-harmonic generation

ABSTRACT

The coherent superposition of two vortex beams with opposite topological charges gives rise to the formation of petal-like beams with unique intensity profiles and azimuthal phase structures, offering great potential for various applications. Here, the generation of anisotropic second-harmonic petal-like beams is demonstrated using ultrathin niobium oxide dibromide ($NbOBr_2$) holograms. The polarization-dependent Raman measurements are conducted on the $NbOBr_2$ flake to reveal the anisotropic properties of the crystal. By imprinting the beam profile information of the superposed vortex beams on the designed $NbOBr_2$ holograms, highly anisotropic second-harmonic petal-like beams with different combinations of the topological charges of vortex beams are produced. The results demonstrated here provide a pathway toward the development of chip-scale polarization-sensitive functional optical devices for applications in optical communication, optical trapping, and quantum optics.

1 | Introduction

The Laguerre–Gaussian (LG) beam is often known as a vortex beam characterized by an integer value of the topological charge l, carrying the associated orbital angular momentum (OAM) of $l\hbar$ per photon. Generally, LG beams can be represented with two integers of p and l as LG_{pl}, where p (≥ 0) and l are the radial and azimuthal indices, respectively. For $p = 0$, the LG beam has a characteristic intensity profile of single-ringed donut shape and a helical phase front with the azimuthal phase dependence of $\exp(il\phi)$. LG beams form a complete set of orthogonal modes which are solutions to the paraxial wave equation. The OAM provides an additional degree of freedom, making vortex beams promising candidates for significantly boosting the information-carrying capacity in optical communication [1–3]. Besides, the generation of vortex beams has attracted significant interests in a wide range of applications including optical trapping and manipulation [4–7], quantum entanglement [8, 9], vortex lasing [10, 11], and optical imaging [12, 13]. Most widely used methods for generating vortex beams, such as spatial light modulators and spiral phase plates, are bulky and not compatible with on-chip integration. The generation of vortex beams has been demonstrated in integrated photonic platforms such as metasurfaces and holography-based devices [14–18]. The coherent superposition of two vortex beams with different radial and azimuthal indices results in the so-called petal-like beams featuring distinctive intensity profile and azimuthal phase dependence due to the two-beam interference effects in the azimuthal direction, which offer great potential for utilization in optical trapping of particles, cold atoms, and Bose–Einstein condensates [19–24]. The spatial intensity variation in the petal-like beam produces periodic energy potential wells, so that the target objects can be trapped in either high- or low-intensity regions. In addition, these composite petal-like beams have been utilized in other applications such as tighter focusing of light [24], ultrasensitive angular measurement [25], and spinning object detection [26]. Meanwhile, the generation of the petal-like beam or other structured beams in the nonlinear regime offers advantages over the beam generation in the linear regime for the realization of all-optical switching and wavelength conversion for wavelength division multiplexing based on nonlinear optical processes such as harmonic generation and spontaneous parametric down-conversion [27–29]. Frequency conversion of structured beams using second-harmonic generation (SHG) allows optical trapping of certain atoms with transition energies not directly accessible by the laser frequencies [30]. The second-order nonlinear optical process is also essential for entangled photon pair generation used for quantum information processing with the photons being entangled in various degrees of freedom including polarization and spatial mode [8, 25, 31].

On the other hand, two-dimensional (2D) van der Waals materials have garnered tremendous research interest due to their versatile optical, electrical, thermal, and mechanical properties. In the context of nonlinear optics, different families of 2D materials have been extensively studied for their strong and tailorable responses in harmonic generation, wave mixing process, and nonlinear absorption, paving the way for building functional optical devices in diverse applications such as optical communication [32, 33], optical sensing [34], ultrafast photonics [35, 36], and quantum information technologies [37, 38]. Highly anisotropic linear and nonlinear optical properties of different kinds of 2D materials due to low in-plane crystal symmetry have been reported, which hold great potential for realizing ultracompact polarization-sensitive optical devices [39–41]. In this context, ferroelectric niobium oxide dihalides ($NbOX_2$, X = Cl, Br, I) are a new group of materials that have gained significant attention due to their strong, anisotropic, and tunable SHG responses [42–44]. In the case of $NbOBr_2$ crystal, an ultrathin flake is observed to generate the SHG power with the same order of magnitude as a monolayer MoS_2, while the SHG power in $NbOBr_2$ crystal scales quadratically with the flake thickness which provides a large SHG tunability range useful for practical device applications [44]. The strong SHG response of $NbOX_2$ crystals can be associated with the ferroelectricity of these materials, with the generated spontaneous polarization along the polar axis of the crystal and the simultaneous breaking of the inversion symmetry. The SHG response of $NbOX_2$ crystals can also be tuned by external stimuli such as temperature, pressure, and strain, which offer significant promise for the realization of optical sensing and switching devices [42, 45–49].

In this work, we demonstrate the generation of anisotropic second-harmonic petal-like beams using the grating holograms patterned on $NbOBr_2$ thin flakes. First, the $NbOBr_2$ crystal is characterized to study the polarization-dependent Raman and SHG responses for revealing strong anisotropic optical properties of the crystal. Next, the designed grating holograms are patterned on ultrathin $NbOBr_2$ flakes which imprint the beam profile information of the superposed vortex beams with opposite topological charges. The second-harmonic petal-like beams with two different combinations of topological charges $|l| = 2$ and $|l| = 4$ are produced in the Fourier plane at the first diffraction order. Highly anisotropic responses in the SHG intensities of the generated petal-like beams are observed, which are attributed to the unique anisotropic crystal structure of the $NbOBr_2$ lattice. Furthermore, the relative magnitudes of the second-order nonlinear susceptibility tensor elements of the $NbOBr_2$ crystal are extracted from the polarization-dependent SHG measurements. These results provide new opportunities for the development of future nonlinear integrated photonic devices, which will enable many promising applications including optical communication, optical trapping, optical sensing, and quantum optics.

2 | Results and Discussion

The crystal structure of $NbOBr_2$ is illustrated in Figure 1a. The crystal has a monoclinic structure belonging to C2 space group, exhibiting a 1D Peierls distortion with the unequal spacings between two Nb atoms ($L_1 \neq L_2$) along the *c*-axis and the unequal spacings of an Nb atom from two O atoms ($D_1 \neq D_2$) along the *b*-axis. This breaks the crystal's inversion symmetry and creates a spontaneous polarization along the *b*-axis also known as the polar axis. The $NbOBr_2$ crystal exhibits strong anisotropic optical properties due to its low in-plane symmetry. First, polarization-resolved Raman measurements are conducted to understand the anisotropic Raman response behavior of the $NbOBr_2$ crystal. Figure 1b,c present the optical microscope image and the atomic force microscopy (AFM) image of one exfoliated $NbOBr_2$ flake on a glass substrate. According to the line scan of the AFM image shown in Figure 1c, the thickness of the flake is estimated to be ≈102 nm. The parallel and perpendicular components of the Raman spectra are shown as contour plots in Figure 1d,e when the linear polarization angle of the excitation beam is rotated. A total of six distinct Raman modes are observed, with all the modes displaying pronounced anisotropic behavior. To better understand the polarization-dependent Raman intensities, the parallel and perpendicular components for each Raman mode are presented as polar plots in Figure 2. The Raman modes at 125, 131, 239, 274, and 649 cm^{-1} plotted in Figure 2a–e are attributed to the A_g modes, while the Raman mode at 201 cm^{-1} plotted in Figure 2f corresponds to the B_g mode. The parallel components of the Raman modes at 125, 131, and 649 cm^{-1} have their maxima along the crystallographic *b*-axis with secondary maxima occurring along the *c*-axis, whereas the Raman modes at 239 cm^{-1} and 274 cm^{-1} have their maxima along the *c*-axis and secondary maxima along the *b*-axis. The perpendicular components of all the A_g modes have four-lobe profiles with maxima occurring approximately along 45° with respect to the *b*- and *c*-axes. Both the parallel and perpendicular components of the B_g mode at 201 cm^{-1} have four-lobe profiles, with the parallel component having maxima along 45° to the *b*- and *c*-axes and the perpendicular component exhibiting maxima along the *b*- and *c*-axes. For $NbOBr_2$ belonging to monoclinic C2 crystal structure, the parallel and perpendicular components of the Raman intensities for the A_g and B_g modes can be written as:

$$I_{\parallel}\left(A_g\right) \propto |a|^2 cos^4\theta + |b|^2 sin^4\theta + \frac{|a||b|}{2} cos\phi_{ab} sin^2 2\theta, \qquad (1)$$

$$I_{\perp}\left(A_g\right) \propto \frac{1}{4}\left(|a|^2 + |b|^2 - 2|a||b| cos\phi_{ab}\right) sin^2 2\theta, \qquad (2)$$

$$I_{\parallel}\left(B_g\right) \propto |f|^2 sin^2 2\theta, \qquad (3)$$

$$I_{\perp}\left(B_g\right) \propto |f|^2 cos^2 2\theta, \qquad (4)$$

where a, b, and f are the elements of the Raman tensor, and ϕ_{ab} is the phase difference between a and b. The excitation polarization angle θ is defined relative to the crystallographic *c*-axis. The theoretical fits are plotted in Figure 2 as red solid lines, showing

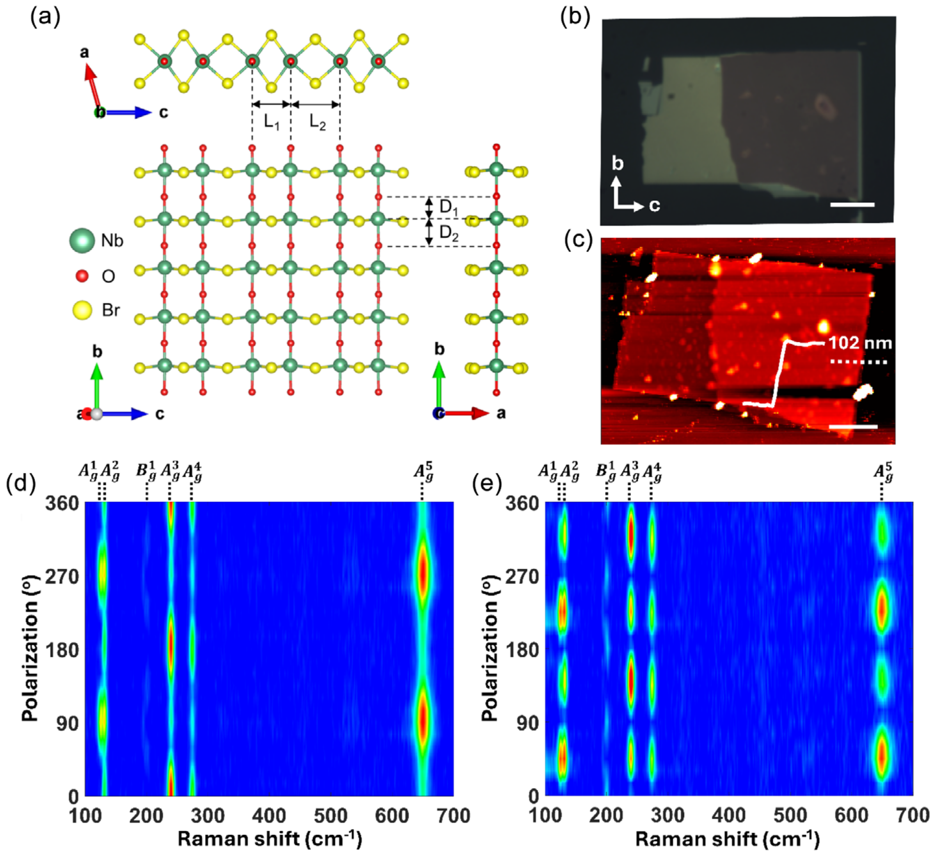

FIGURE 1 | (a) Schematic illustration of the crystal structure of $NbOBr_2$. (b) Optical microscope image of the 102 nm-thick $NbOBr_2$ flake on a glass substrate. Crystallographic *b*- and *c*-axes of the flake are labeled. (c) AFM image of the flake with the line scan plotted in the inset. All scale bars are 20 µm. Contour plots of (d) parallel component, and (e) perpendicular component of the polarization-resolved Raman intensities.

good agreement with the experimental results shown as blue dots.

The anisotropic optical properties of the $NbOBr_2$ crystal are further studied with simultaneous polarization-resolved measurements of Raman and SHG intensities. Figure 3a, b display the optical microscope image and the AFM image of an exfoliated flake, with the thickness of 82 nm determined from the line scan of the AFM image. The parallel component of the polarization-resolved Raman intensity for the A_g mode at 649 cm^{-1} is plotted in Figure 3c, showing that the maximum intensity occurs along the *b*-axis which is consistent with the measurements presented in Figure 2e for the flake displayed in Figure 1. The theoretical fit is also shown in Figure 3c giving good agreement with the experimental data. Next, polarization-resolved SHG response of the $NbOBr_2$ flake is characterized at the excitation wavelength of 1560 nm. Figure 3d shows the measured nonlinear signal depending on the excitation power, giving a slope of 1.99 in the power law fit which is the evidence of the SHG process. Figure 3e shows the SHG spectrum depicting a peak at 780 nm which is half of the excitation wavelength, further confirming the SHG process. The polarization-dependent SHG responses for the parallel and perpendicular components and the total SHG intensity are shown in Figure 3f, as the excitation linear polarization angle is rotated in the crystallographic *bc*-plane with the propagation of the excitation beam along the direction perpendicular to the *bc*-plane. Both the parallel and perpendicular components have two-lobe profiles, where the parallel component has the maximum SHG intensity along the *b*-axis and the perpendicular component has the maximum intensity along the *c*-axis. The perpendicular component is significantly weaker than the parallel component, which leads to the total SHG intensity having a two-lobe profile with the maximum intensity occurring along the *b*-axis. For $NbOBr_2$ crystal belonging to monoclinic C2 crystal structure, the parallel and perpendicular components of SHG intensity can be expressed as:

$$I_{2\omega}^{\parallel} \propto |3\chi_{bcc}^{(2)}cos^2\theta sin\theta + \chi_{bbb}^{(2)}sin^3\theta|^2, \tag{5}$$

$$I_{2\omega}^{\perp} \propto |\chi_{bcc}^{(2)}cos^3\theta - 2\chi_{bcc}^{(2)}sin^2\theta cos\theta + \chi_{bbb}^{(2)}sin^2\theta cos\theta|^2, \tag{6}$$

where $\chi_{bbb}^{(2)}$ and $\chi_{bcc}^{(2)}$ are the elements of the second-order nonlinear susceptibility tensor, and θ is the polarization angle of the excitation beam with respect to the crystallographic *c*-axis. The theoretical fits are plotted in Figure 3f as solid lines showing good agreement with the measurements. It is noted that $\chi_{bbb}^{(2)}$ has a larger value compared to $\chi_{bcc}^{(2)}$ at the excitation wavelength, leading to a strong anisotropic SHG response with the maximum intensity occurring along the *b*-axis. From the above results, it is demonstrated that both polarization-resolved Raman and SHG measurements are effective tools to identify the crystallographic orientations of $NbOBr_2$ thin flakes.

The grating holograms are designed to produce second-harmonic petal-like beams by imprinting the beam structure information of

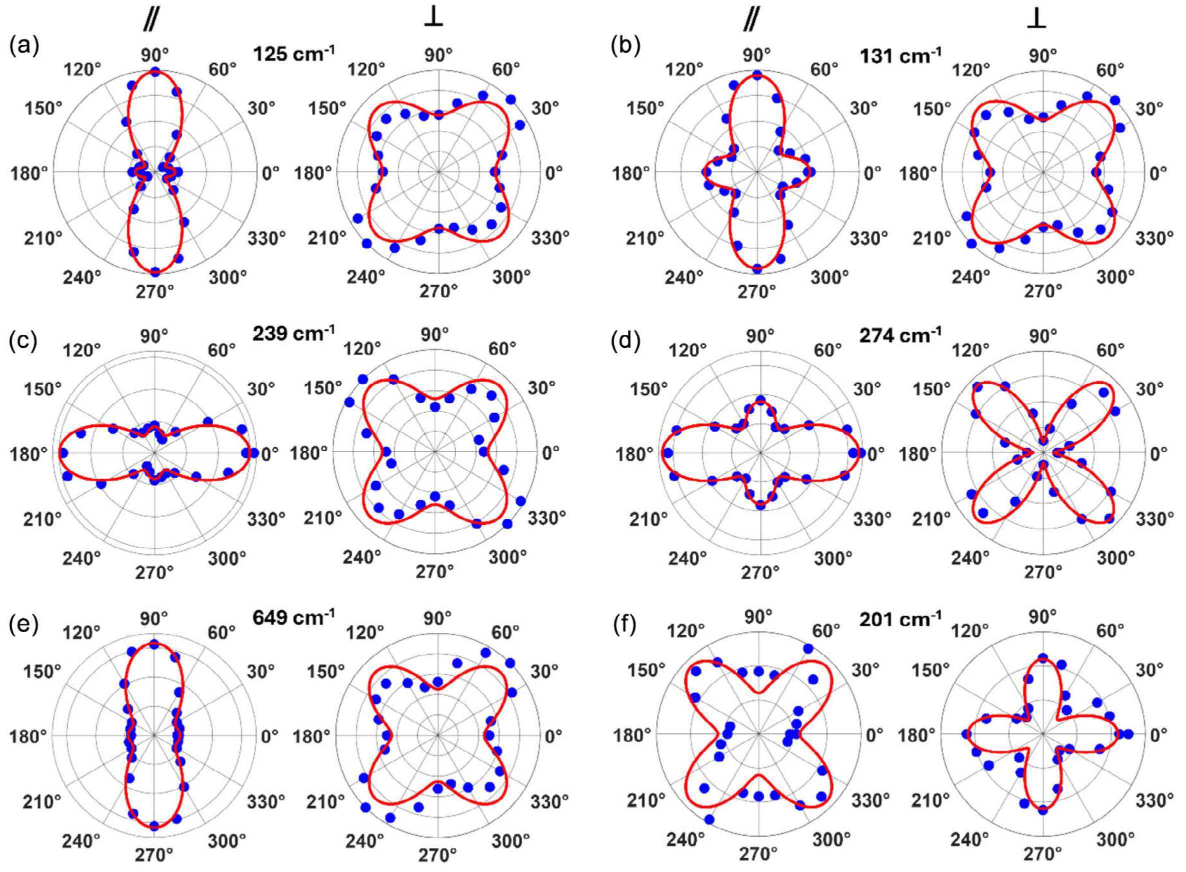

FIGURE 2 | Polar plots of the polarization-resolved Raman intensities of the parallel and perpendicular components from the 102 nm-thick $NbOBr_2$ flake for (a–e) the A_g modes at 125, 131, 239, 274, and 649 cm^{-1}, and (f) the B_g mode at 201 cm^{-1}. Red solid lines are theoretical fits to the experimental data shown as blue dots. The crystallographic *b*-axis is aligned along the vertical direction.

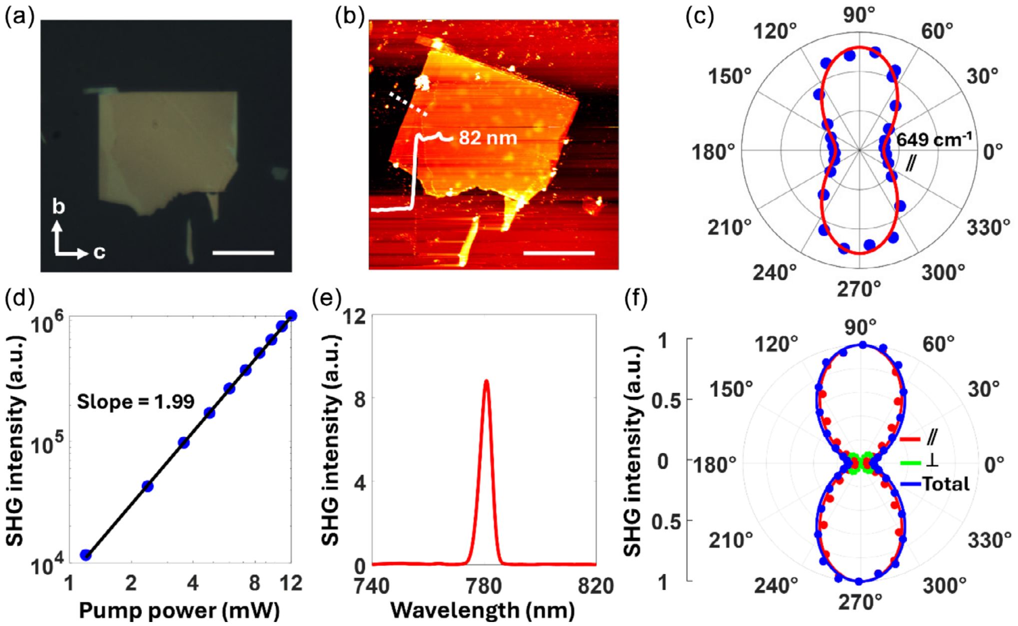

FIGURE 3 | (a) Optical microscope image of the 82 nm-thick $NbOBr_2$ flake with the crystallographic *b*- and *c*-axes labeled. (b) AFM image of the flake with the line scan plotted in the inset. All scale bars are 20 μm. (c) Parallel component of the polarization-resolved Raman intensity for the A_g mode at 649 cm^{-1}. Red solid line is the theoretical fit to the experimental data shown as blue dots. (d) SHG intensity as a function of the excitation power in log–log plot. (e) SHG spectrum measured from the flake. (f) Parallel component, perpendicular component, and total intensity of the polarization-resolved SHG signal shown as red, green, and blue dots, respectively, with the theoretical fits depicted as solid lines.

the superposed vortex beams with opposite topological charges on the NbOBr$_2$ crystal. Here, the equally weighted superposition of two LG beams of LG$_{0l}$ and LG$_{0\text{-}l}$ with the same radial index of $p = 0$ and the opposite topological charges of l and $-l$ is considered to generate the composite petal-like beam carrying no net OAM and forming $2|l|$ intensity lobes or petals along the azimuthal direction. The binary amplitude modulation of the second-order nonlinear susceptibility required in the NbOBr$_2$ crystal to generate a second-harmonic vortex beam with topological charge l can be expressed as:

$$\chi_l^{(2)}(x,y) = \chi^{(2)}\left\{\frac{1}{2} + \frac{1}{2}sgn\left[cos\left\{\frac{2\pi x}{\Lambda} - \phi(x,y)\right\} - cos\left\{sin^{-1}A(x,y)\right\}\right]\right\}, \tag{7}$$

with the following phase profile:

$$\phi(x,y) = \begin{cases} l \cdot tan^{-1}(y/x) & x \geq 0 \\ l \cdot [tan^{-1}(y/x) + \pi] & x < 0 \end{cases} \tag{8}$$

and the amplitude profile $A(x,\ y) = 1$. Λ is the grating period which is selected as 3 μm in the design. To generate the petal-like beam from the coherent superposition of two vortex beams with the opposite topological charges of l and $-l$, the product of binary amplitude modulation functions of the two vortex beams is considered as:

$$\chi_{petal}^{(2)}(x,y) = \chi_l^{(2)}(x,y) \cdot \chi_{-l}^{(2)}(x,y). \tag{9}$$

The generated second-harmonic petal-like beams will appear in the first diffraction order. Using the grating equation $\theta_{SHG} = sin^{-1}(\lambda_{SHG}/\Lambda)$, the diffraction angle θ_{SHG} is calculated as ≈15.1° based on the SHG wavelength λ_{SHG} of 780 nm and the grating period Λ of 3 μm. The designed grating holograms are patterned on the NbOBr$_2$ flakes using focused ion beam (FIB) milling. Figure 4a,b show the scanning electron microscopy (SEM) image and the optical microscope image of the fabricated hologram with the grating lines oriented along the crystallographic *c*-axis for producing the petal-like beam with the combination of topological charges $|l| = 2$. Before the FIB milling, the AFM measurement is performed on the NbOBr$_2$ flake to determine the thickness of the flake as 60 nm, as shown in the line scan plot of the AFM image depicted in the inset of Figure 4b. Figure 4c displays the SHG image of the grating hologram in the real plane with the excitation beam at the wavelength of 1560 nm. Figure 4d shows the corresponding SHG image in the Fourier plane, which demonstrates the production of the second-harmonic petal-like beams in the first diffraction order. The generated petal-like beams in the +1 and −1 diffraction

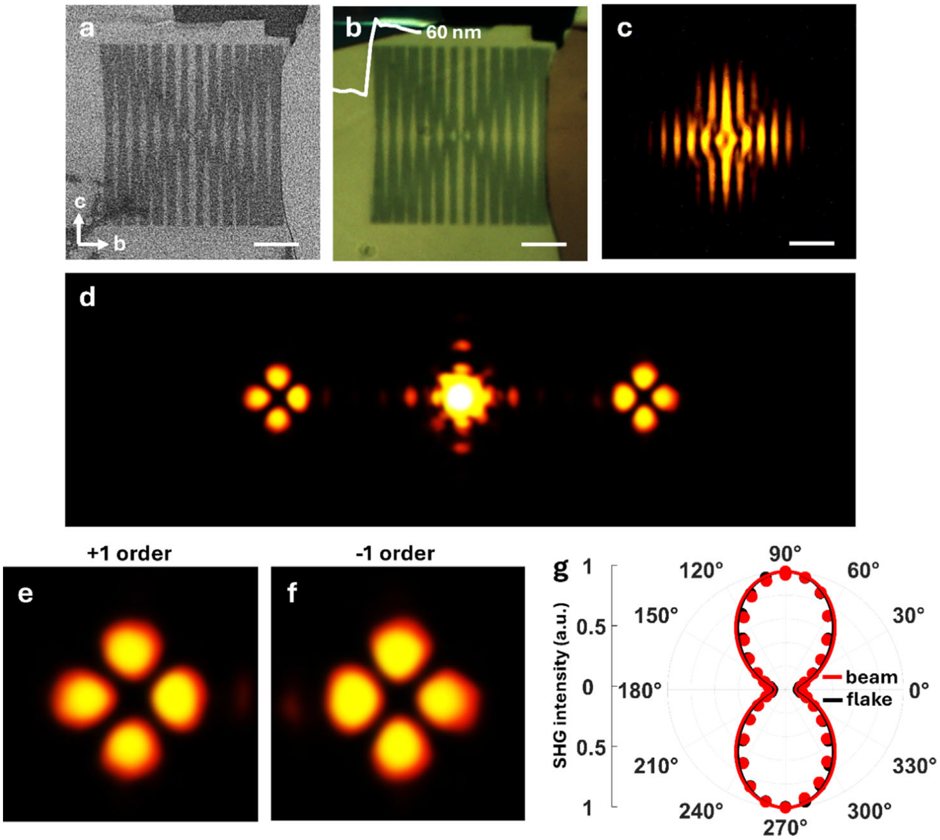

FIGURE 4 | Generation of second-harmonic petal-like beam with $|l| = 2$ using NbOBr$_2$ grating hologram. (a) SEM image of the hologram with the crystallographic *b*- and *c*-axes labeled. (b) Optical microscope image of the hologram with the line scan plot of the AFM image in the inset. (c) SHG image of the hologram in the real plane. All scale bars are 10 μm. (d) SHG image in the Fourier plane demonstrating the generation of the petal-like beams in the first diffraction order. (e and f) The individual petal-like beams in the +1 diffraction order and the −1 diffraction order, respectively. (g) Polarization-dependent SHG intensities of the petal-like beam and the bare flake plotted as red and black dots, respectively. Solid lines are the theoretical fits to the experimental data.

orders are further plotted separately in Figure 4e, f. Both beams exhibit the four-lobe intensity profiles with four intensity maxima and four intensity minima alternatively occurring along the azimuthal direction, which is a consequence of the two-beam interference effects from the superposed vortex modes. By considering the superposition of two vortex modes with equal amplitudes and different topological charges of l_1 and l_2, the complex amplitude function can be expressed as $U = \exp(il_1\phi) + \exp(il_2\phi)$ where ϕ is the azimuthal angle. The superposed field can be written as $U = 2\cos(\frac{l_1 - l_2}{2}\phi) \cdot \exp(i\frac{l_1 + l_2}{2}\phi)$. By considering the opposite topological charges of $l_1 = l$ and $l_2 = -l$, the transverse intensity profile of the superposed beam follows a dependence of $\cos^2(l\phi)$ along the azimuthal direction, exhibiting $2|l|$ intensity petals separated by $2|l|$ zero crossings of the intensity due to the interference between the two vortex modes. The phase term indicates that there is no net angular momentum carried by the superposed beam, but the azimuthal phase structure of the beam exhibits the phase of 0 or π at the intensity peaks while the phase at the zero-intensity regions between the petals switches between 0 and π. Next, the polarization angle–dependent SHG measurements are performed on the petal-like beam to study its anisotropic response, which is plotted in Figure 4g as red dots. A two-lobe profile is observed with the maximum SHG intensity occurring along the *b*-axis of the crystal. For comparison, the polarization angle–dependent SHG response for the bare flake is included in Figure 4g as black dots. The theoretical fits obtained using Equations (5), (6) are also plotted in Figure 4g depicted as solid red and black lines for the petal-like beam and the bare flake, respectively, showing a good agreement with the measurements. The measured SHG anisotropy ratios described by the ratio between the maximum and minimum intensities are 8.98 and 7.93 for the bare flake and the petal-like beam, respectively. The variations in the SHG anisotropy ratios of the hologram compared to the flake may be attributed to the fabrication-induced defects in the $NbOBr_2$ crystal during the FIB milling process with gallium ions. The gallium ion contamination can change the $NbOBr_2$ lattice structure and electronic properties, which will alter the second-order nonlinear susceptibility tensor elements and thus the SHG anisotropy ratio [49].

The grating hologram is further designed to generate the second-harmonic petal-like beam with the combination of higher topological charges $|l| = 4$. Figure 5a,b show the SEM image and the optical microscope image of the patterned hologram with the grating lines oriented along the crystallographic *b*-axis. According to the line scan plot of the AFM image shown in the inset of Figure 5b, the thickness of the $NbOBr_2$ flake is estimated as 58 nm. The SHG images obtained in the real plane and the Fourier plane are presented in Figure 5c,d, demonstrating the generation of the petal-like beams in the first diffraction order. The individual petal-like beams in the +1 and −1 diffraction orders are displayed in Figure 5e,f, showing eight well-defined intensity petals due to

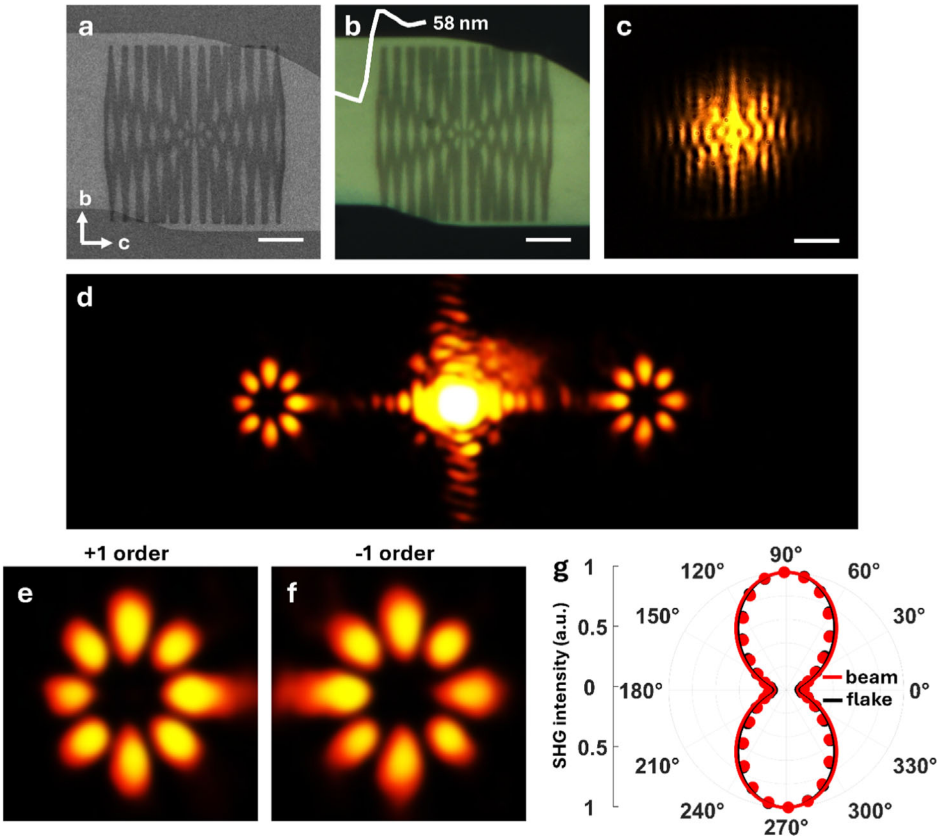

FIGURE 5 | Generation of second-harmonic petal-like beam with $|l| = 4$ using $NbOBr_2$ grating hologram. (a) SEM image of the hologram. (b) Optical microscope image of the hologram with the line scan plot of the AFM image in the inset. (c) SHG image of the hologram in the real plane. All scale bars are 10 μm. (d) SHG image in the Fourier plane showing the generation of the petal-like beam in the first diffraction order. (e and f) The individual petal-like beams in the +1 and −1 diffraction orders. (g) Polarization-dependent SHG intensities of the petal-like beam and the bare flake plotted as red and black dots, respectively. Solid lines are the theoretical fits to the experimental data.

the unique azimuthal phase structure of the superposed vortex modes with topological charges $|l| = 4$. Subsequently, the measured polarization-dependent SHG response of the petal-like beam is plotted in Figure 5g as red dots, showing highly anisotropic response with the maximum SHG intensity occurring along the *b*-axis of the crystal. The polarization-dependent SHG response of the bare flake is also plotted in Figure 5g as black dots. The measured SHG anisotropy ratios for the bare flake and the petal-like beam are 8.33 and 7.45, respectively. The theoretical fits are also plotted in Figure 5g as solid lines, giving a good agreement with the experimental data.

In addition, the SHG conversion efficiencies of the generated petal-like beams are determined. The excitation polarization is aligned with the crystallographic *b*-axis for achieving the maximum SHG intensity. An average excitation power of 60 mW is used for the SHG measurements with a laser spot diameter of 45 μm, giving a peak excitation irradiance of 0.52 GW/cm^2 on the hologram. The SHG conversion efficiency of the petal-like beam is defined as $\eta_{\mathrm{CE}} = \eta_{\mathrm{SHG}} \cdot \eta_{\mathrm{DE}}$, where η_{SHG} is the SHG conversion efficiency of the hologram, and η_{DE} is the diffraction efficiency of the petal-like beam in the ±1 diffraction order. η_{SHG} is determined by the ratio of the total SHG power generated from the hologram to the excitation power of the fundamental beam, and the calculated conversion efficiencies of the holograms are 1.20×10^{-10} and 9.63×10^{-11} for producing the petal-like beams with $|l| = 2$ and $|l| = 4$, respectively. η_{DE} is calculated as the fraction of total SHG power directed toward the ±1 diffraction order. The diffraction efficiencies of the petal-like beams with $|l| = 2$ and $|l| = 4$ are calculated as 49.57% and 55.48%, respectively. The SHG conversion efficiencies of the generated petal-like beams with $|l| = 2$ and $|l| = 4$ are then determined as 5.95×10^{-11} and 5.34×10^{-11}, respectively. It is noteworthy that the SHG conversion efficiencies of the NbOBr$_2$, NbOI$_2$, and NbOCl$_2$ thin crystals have the same order of magnitude in 10^{-11} to 10^{-10} at the peak excitation irradiance of ≈1 GW/cm^2 [49, 50], which is much higher than the SHG conversion efficiency of a monolayer MoS$_2$ [51]. Moreover, the relative magnitudes of the independent second-order nonlinear susceptibility tensor elements are retrieved from the theoretical fits of the polarization-dependent SHG measurements using Equations (5), (6), as listed in Table 1 for the bare flakes and the petal-like beams. The $\chi^{(2)}_{bcc}$ value is found to be in the range of 0.33–0.36 relative to the $\chi^{(2)}_{bbb}$ value which is set to unity. The theoretical SHG anisotropy ratio can be calculated as $|\chi^{(2)}_{bbb}/\chi^{(2)}_{bcc}|^2$, which varies from 7.72 to 9.18 for the samples. It shows that the theoretical SHG anisotropy ratio is consistent with the measured SHG anisotropy ratio, ranging from 7.45 to 8.98, as summarized in Table 1.

TABLE 1 | Summary of the retrieved second-order nonlinear susceptibility tensor elements of NbOBr$_2$ crystal as well as the theoretical and measured SHG anisotropy ratios for the flakes and the holograms.

Sample	$\chi^{(2)}_{bbb}$	$\chi^{(2)}_{bcc}$	$\lvert\chi^{(2)}_{bbb}/\chi^{(2)}_{bcc}\rvert^2$	Measured anisotropy ratio
Flake 1	1	0.33	9.18	8.98
$\lvert l\rvert = 2$	1	0.35	8.16	7.93
Flake 2	1	0.34	8.65	8.33
$\lvert l\rvert = 4$	1	0.36	7.72	7.45

3 | Conclusion

In summary, we have demonstrated the generation of highly anisotropic second-harmonic petal-like beams using the designed grating holograms patterned on NbOBr$_2$ thin flakes. The NbOBr$_2$ crystal is characterized by the polarization-resolved Raman and SHG measurements to reveal the strong anisotropic optical responses of the crystal, which can also be utilized as effective tools to identify the crystallographic orientations of NbOBr$_2$ thin flakes. The highly anisotropic second-harmonic petal-like beams with different combinations of topological charges for the superposed vortex modes are generated from the designed NbOBr$_2$ grating holograms. Distinct intensity profiles with well-defined intensity petals and high SHG anisotropy ratios for the generated second-harmonic petal-like beams are observed. The results presented here can be extended to the generation of other types of superposed optical beams based on coherent interference, which makes the 2D material-based holograms a versatile platform capable of producing anisotropic nonlinear optical beams with complex spatial intensity profiles and unique phase structures suitable for a wide range of emerging applications. Our demonstrated results hold promise for the development of future multifunctional polarization-sensitive optical devices used for applications in integrated photonics, optical communication, optical trapping, and quantum optics.

4 | Experimental Section

4.1 | Sample Preparation

NbOBr$_2$ flakes are mechanically exfoliated from bulk crystal (Nanjing MKNANO Tech. Co., Ltd.) to polydimethylsiloxane layers using scotch tape and then transferred to glass substrates. The substrates are cleaned using acetone and isopropyl alcohol before the transfer. The holograms are patterned using FIB (FEI Helios Nanolab 600) with the patterned area of $40 \times 40\ \mu\mathrm{m}^2$. A conductive polymer layer is spin coated on top of the flake for surface charge dissipation during the FIB milling. The sample is then rinsed with deionized water to remove the conductive polymer layer and blown dry with nitrogen gas.

4.2 | Optical Setup

The Raman measurements are performed using a 632.8 nm He–Ne laser, and the laser beam is focused on the sample using a 60× objective lens (NA = 0.85). The back-reflected signal is directed to an optical spectrometer (Horiba, iHR550) after passing through a 633 nm ultrasteep longpass edge filter (Semrock, LP02-633RE-25). For polarization-resolved measurements, the excitation and detection polarizations are simultaneously rotated by using a half-wave plate and a linear polarization analyzer, respectively. For SHG measurements, the linearly polarized 1560 nm pump laser beam (Calmer fiber laser, pulse width 90 fs, repetition rate 80 MHz) is focused on the sample using a 4× objective lens (NA = 0.12). A half-wave plate is used to rotate the linear polarization of the excitation beam. The transmitted signal is collected by a 20× objective lens (NA = 0.42) and passed through a set of 900 nm shortpass filter and 780 nm bandpass filter to selectively detect the SHG signal. The SHG images of the hologram in the real plane and the Fourier plane are then recorded using a color charge-coupled device camera. The SHG spectrum is acquired using the optical spectrometer.

Acknowledgments

The authors acknowledge the support from the National Science Foundation under Grant Nos. DMR-2412218, DMR-2412219, ECCS-2226875, and ECCS-2226948. The authors thank the facility support from the Materials Research Center at Missouri S&T.

Conflict of Interest

The authors declare no conflicts of interest.

Data Availability Statement

The data that support the findings of this study are available from the corresponding author upon reasonable request.

References

1. A. E. Willner, H. Huang, Y. Yan, et al., "Optical Communications Using Orbital Angular Momentum Beams," *Advances in Optics and Photonics* 7 (2015): 66.

2. J. Wang, "Advances in Communications Using Optical Vortices," *Photonics Research* 4 (2016): B14.

3. J. Liu, J. Zhang, J. Liu, et al., "1-Pbps Orbital Angular Momentum Fibre-Optic Transmission," *Light: Science & Applications* 11 (2022): 202.

4. M. Padgett and R. Bowman, "Tweezers with a Twist," *Nature Photonics* 5 (2011): 343.

5. C. T. Schmiegelow, J. Schulz, H. Kaufmann, T. Ruster, U. G. Poschinger, and F. Schmidt-Kaler, "Transfer of Optical Orbital Angular Momentum to a Bound Electron," *Nature Communications* 7 (2016): 12998.

6. S. Franke-Arnold, "Optical Angular Momentum and Atoms," *Philosophical Transactions of the Royal Society A: Mathematical, Physical and Engineering Sciences* 375 (2017): 20150435.

7. Y. Shen, X. Wang, Z. Xie, et al., "Optical Vortices 30 years on: OAM Manipulation from Topological Charge to Multiple Singularities," *Light: Science & Applications* 8 (2019): 90.

8. Y. Zhang, M. Agnew, T. Roger, et al., "Simultaneous Entanglement Swapping of Multiple Orbital Angular Momentum States of Light," *Nature Communications* 8 (2017): 632.

9. C. Wu, S. Kumar, Y. Kan, et al., "Room-Temperature on-Chip Orbital Angular Momentum Single-Photon Sources," *Science Advances* 8 (2022): eabk3075.

10. C. Huang, C. Zhang, S. Xiao, et al., "Ultrafast Control of Vortex Microlasers," *Science (New York, N.y.)* 367 (2020): 1018.

11. A. Forbes, L. Mkhumbuza, and L. Feng, "Orbital Angular Momentum Lasers," *Nature Reviews Physics* 6 (2024): 352.

12. Y. Kozawa, D. Matsunaga, and S. Sato, "Superresolution Imaging via Superoscillation Focusing of a Radially Polarized Beam," *Optica* 5 (2018): 86.

13. J. Zeng, Y. Dong, Y. Wang, J. Zhang, and J. Wang, "Optical Imaging Using Orbital Angular Momentum: Interferometry, Holography and Microscopy," *Journal of Lightwave Technology* 41 (2023): 2025.

14. X. Ma, M. Pu, X. Li, et al., "A Planar Chiral Meta-Surface for Optical Vortex Generation and Focusing," *Scientific Reports* 5 (2015): 10365.

15. B. Liu, Y. He, S-Wai Wong, and Y. Li, "Multifunctional Vortex Beam Generation by a Dynamic Reflective Metasurface," *Advanced Optical Materials* 9 (2021): 2001689.

16. Q. Chen, G. Qu, J. Yin, et al., "Highly Efficient Vortex Generation at the Nanoscale," *Nature Nanotechnology* 19 (2024): 1000.

17. A. Liu, C.-L. Zou, X. Ren, Q. Wang, and G.-C. Guo, "On-Chip Generation and Control of the Vortex Beam," *Applied Physics Letters* 108 (2016): 181103.

18. H. Ahmed, H. Kim, Y. Zhang, et al., "Optical Metasurfaces for Generating and Manipulating Optical Vortex Beams," *Nanophotonics* 11 (2022): 941.

19. S. Franke-Arnold, J. Leach, M. J. Padgett, et al., "Optical Ferris Wheel for Ultracold Atoms," *Optics Express* 15 (2007): 8619.

20. S. Huang, Z. Miao, C. He, F. Pang, Y. Li, and T. Wang, "Composite Vortex Beams by Coaxial Superposition of Laguerre–Gaussian Beams," *Optics and Lasers in Engineering* 78 (2016): 132.

21. V. Shahabadi and E. Madadi, "Effective Multiple Optical Trapping of Sub-Micrometer Particles with Petal Beams," *Journal of the Optical Society of America B* 37 (2020): 3665.

22. I. Moreno, J. A. Davis, T. Womble-Dahl, and D. M. Cottrell, "Azimuthal Multiple-Beam Interference Effects with Combinations of Vortex Beams," *Optics Letters* 40 (2015): 2341.

23. I. A. Litvin, L. Burger, and A. Forbes, "Angular Self-Reconstruction of Petal-Like Beams," *Optics Letters* 38 (2013): 3363.

24. P. Woźniak, P. Banzer, F. Bouchard, E. Karimi, G. Leuchs, and R. W. Boyd, "Tighter Spots of Light with Superposed Orbital-Angular-Momentum Beams," *Physical Review. A, Atomic, Molecular, and Optical Physics* 94 (2016): 021803.

25. V. D'Ambrosio, N. Spagnolo, L. D. Re, et al., "Photonic Polarization Gears for Ultra-Sensitive Angular Measurements," *Nature Communications* 4 (2013): 2432.

26. M. P. J. Lavery, F. C. Speirits, S. M. Barnett, and M. J. Padgett, "Detection of a Spinning Object Using Light's Orbital Angular Momentum," *Science (New York, NY)* 341 (2013): 537.

27. W. T. Buono and A. Forbes, "Nonlinear Optics with Structured Light," *Opto-Electronic Advances* 5 (2022): 210174.

28. A. Dasgupta, J. Gao, and X. Yang, "Second-Harmonic Optical Vortex Conversion from WS_2 Monolayer," *Scientific Reports* 9 (2019): 8780.

29. A. Sinelnik, S. H. Lam, F. Coviello, et al., "Ultrafast All-Optical Second Harmonic Wavefront Shaping," *Nature Communications* 15 (2024): 2507.

30. F. Theron, Y. Bidel, E. Dieu, N. Zahzam, M. Cadoret, and A. Bresson, "Frequency-Doubled Telecom Fiber Laser for a Cold Atom Interferometer Using Optical Lattices," *Optics Communications* 393 (2017): 152.

31. A. Mair, A. Vaziri, G. Weihs, and A. Zeilinger, "Entanglement of the Orbital Angular Momentum States of Photons," *Nature* 412 (2001): 313.

32. A. Autere, H. Jussila, Y. Dai, Y. Wang, H. Lipsanen, and Z. Sun, "Nonlinear Optics with 2D Layered Materials," *Advanced Materials (Deerfield Beach, Fla.)* 30 (2018): 1705963.

33. C.-Y. Zhu, Z. Zhang, J.-K. Qin, et al., "Two-Dimensional Semiconducting SnP_2Se_6 with Giant Second-Harmonic-Generation for Monolithic on-Chip Electronic-Photonic Integration," *Nature Communications* 14 (2023): 2521.

34. R. Yu, J. D. Cox, and F. J. G. de Abajo, "Nonlinear Plasmonic Sensing with Nanographene," *Physics Review Letters*117 (2016): 123904.

35. J. Du, Q. Wang, G. Jiang, et al., "Ytterbium-Doped Fiber Laser Passively Mode Locked by Few-Layer Molybdenum Disulfide (MoS_2)

Saturable Absorber Functioned with Evanescent Field Interaction," *Scientific Reports* 4 (2014): 6346.

36. Z. Sun, A. Martinez, and F. Wang, "Optical Modulators with 2D Layered Materials," *Nature Photonics* 10 (2016): 227.

37. X. Liu and M. C. Hersam, "2D Materials for Quantum Information Science," *Nature Reviews Materials* 4 (2019): 669.

38. M. Turunen, M. Brotons-Gisbert, Y. Dai, et al., "Quantum Photonics with Layered 2D Materials," *Nature Reviews Physics* 4 (2022): 219.

39. H. Yang, H. Jussila, A. Autere, et al., "Optical Waveplates Based on Birefringence of Anisotropic Two-Dimensional Layered Materials," *ACS Photonics* 4 (2017): 3023.

40. A. Dasgupta, J. Gao, and X. Yang, "Anisotropic Third-Harmonic Generation in Layered Germanium Selenide," *Laser & Photonics Reviews* 14 (2020): 1900416.

41. X. Li, H. Liu, C. Ke, et al., "Review of Anisotropic 2D Materials: Controlled Growth, Optical Anisotropy Modulation, and Photonic Applications," *Laser & Photonics Reviews* 15 (2021): 2100322.

42. Q. Guo, X.-Z. Qi, L. Zhang, et al., "Ultrathin Quantum Light Source with Van der Waals $NbOCl_2$ Crystal," *Nature* 613 (2023): 53.

43. I. Abdelwahab, B. Tilmann, Y. Wu, et al., "Giant Second-Harmonic Generation in Ferroelectric $NbOI_2$," *Nature Photonics* 16 (2022): 644.

44. W. D. Chen, S. Zhu, R. H. Duan, et al., "Extraordinary Enhancement of Nonlinear Optical Interaction in $NbOBr_2$ Microcavities," *Advanced Materials (Deerfield Beach, Fla.)* 36 (2024): 2400858.

45. J. R. Fu, N. Z. Yang, Y. Liu, et al., "Emission Dipole and Pressure-Driven Tunability of Second Harmonic Generation in vdWs Ferroelectric $NbOI_2$," *Advanced Functional Materials* 34 (2024): 2308207.

46. M. Huang, W. Chen, S. Luo, Z. Huang, Z. Wang, and X. Qi, "Raman Scattering Evolution in Temperature-Induced Ferroelectric Phase Transition of Few-Layer $NbOCl_2$," *Applied Physics Letters* 124 (2024): 111901.

47. H. Wang, Q. Chen, Y. Cao, et al., "Anisotropic Strain-Tailoring Nonlinear Optical Response in Van der Waals $NbOI_2$," *Nano Letters* 24 (2024): 3413.

48. L. T. Ye, W. J. Zhou, D. J. Huang, et al., "Manipulation of Nonlinear Optical Responses in Layered Ferroelectric Niobium Oxide Dihalides," *Nature Communications* 14 (2023): 5911.

49. J. Deka, X. Yang, and J. Gao, "Anisotropic and Temperature-Tunable Second-Harmonic Vortex Generation in Ferroelectric $NbOCl_2$ Holograms," *Laser & Photonics Reviews* 20 (2026): e01523.

50. J. Deka, J. Gao, and X. Yang, "Anisotropic Second- and Third-Harmonic Hermite-Gaussian Beam Generation with $NbOI_2$ Holograms," *Advanced Photonics Research* 6 (2025): e2500188.

51. R. I. Woodward, R. T. Murray, C. F. Phelan, et al., "Characterization of the Second- and Third-Order Nonlinear Optical Susceptibilities of Monolayer MoS_2 Using Multiphoton Microscopy," *2D Materials* 4 (2017): 011006.